Understanding Powder X-ray Diffraction Profiles from Layered Minerals: The Case of Kaolinite Nanocrystals

Alberto Leonardi[*,†,1] & David L. Bish[2]

1. Department of Earth and Atmospheric Sciences, Indiana University, Bloomington, Indiana 47405, U.S.A.
2. Department of Chemistry, Indiana University, Bloomington, Indiana, 47405, U.S.A.

Layered Minerals, Clays, Kaolinite, Nanocrystal, Layer Stacking, Powder X-ray Diffraction.

SUPPORTING INFORMATION

State of The Art of Line Profile Analysis (LPA) of Powder X-ray Diffraction Data. LPA methods such as Rietveld refinement [1,2] and whole powder pattern modelling (WPPM) [3,4] can account with physical significance only for small deviations of the crystal structure from a well-defined lattice.[5,6] Layer stacking disorder cannot be described with a given structure as it evolves toward the limit of a turbostratic microstructure, in which the in-plane structure of the layers is randomly oriented. Other methods have been suggested to describe the nature of stacking defects. For example, the expert method introduced by Plançon in 1990 provides estimates of several structural characteristics, such as the probability of stacking-fault defects based on the relative position and intensity of a few characteristic peak profiles over a narrow range of scattering angles (i.e., CuKα 2θ range from 18° to 40°).[7] Evolving from the approach first introduced in 2004,[8] Ufer proposed a Rietveld-like approach that uses two distinct crystal structures to independently describe the *00l* and *hkl* reflections.[9,10] The *00l* reflections are influenced only by the persistence of the layer stacking,[11] whereas the *hkl* reflections are affected by the degree of stacking disorder. However, the reliability of the properties estimated by these methods is limited by the effective interpretation of the limited set of diffraction features used in analysis. The more sophisticated BGMN [9,10,12,13], DIFFaX+ [14,15], and CIREALS [16] software approaches model the diffraction profile by a combination of the accurate structure factor of each component in the powder sample. Recursive algorithms attempt then to match experimental data, thereby resolving the characteristic stacking disorder. Some contributions, such as size distribution and shape of the clay nanocrystals or free roto-translation of the layers in the stack, are nonetheless still ignored to facilitate refinement efficiency. The combination of the theoretical algorithm proposed by Drits and Tchoubar in 1990 and a least-squares software application developed by Sakharov and Naumov [17,18] partially addressed such limitations. As an example, although considering crystallite-size distributions, the mean and variance were assumed dependent on each other,[19] limiting the flexibility and reliability of the methodology.

Atom	X	Y	Z
Si (1)	**0.9942**	**0.3393**	**0.0909**
Si (2)	**0.5064**	**0.1665**	**0.9130**
Al (1)	**0.2971**	**0.4957**	**0.4721**
Al (2)	**0.7926**	**0.3300**	**0.4699**
O (1)	**0.0501**	**0.3539**	**0.3170**
O (2)	**0.1214**	**0.6604**	**0.3175**
O (3)	**0.0000**	**0.5000**	**0.0000**
O (4)	**0.2085**	**0.2305**	**0.0247**
O (5)	**0.2012**	**0.7657**	**0.0032**
OH (1)	**0.0510**	**0.9698**	**0.3220**
OH (2)	**0.9649**	**0.1665**	**0.6051**
OH (3)	**0.0348**	**0.4769**	**0.6080**
OH (4)	**0.0334**	**0.8570**	**0.6094**
Space Group C1			
a = 5.1554 Å	**b = 8.9448 Å**		**c = 7.4048 Å**
α = 91.7000°	**β = 104.862°**		**γ = 89.8220°**

Table S1. Kaolinite crystal structure. Unit-cell parameters and relative atom positions refined by Bish & Von Dreele in 1989 for Keokuk kaolinite.[20]

Atom	X	Y	Z	Octahedral Site
Al (1)	**0.2971**	**0.4957**	**0.4721**	**A**
Al (2)	**0.7926**	**0.3300**	**0.4699**	**B**
Al (3)	**0.2949**	**0.1629**	**0.4710**	**C**

Table S2. Octahedral sites. The C octahedral site was derived from the average coordinates of the known Al sites.

Microstructural characteristics of the kaolinite models. The kaolinite structure of **Table S1** was periodically repeated in space to form an infinite single crystal. The ideal sequence of distinct layers was identified. Stacking disorder was than incorporated into the structure by perturbing the configuration of the layers. Stacking-fault defects were otherwise obtained by layer-layer change of the crystal structure, which we refer to as the layers' configuration states. Nanocrystal models were finally obtained selecting those atoms with an imprint within a circular perimeter in-plane with the layers (**Figure S1**).

Four types of layer-layer stacking disorders were incorporated by change of:

i. **Stacking distance (i.e., repeat).** The layers were displaced along the stacking direction normal to the layer plane, not the **c** lattice vector.

ii. Lateral indentation. The circular perimeter used to select atoms from the infinite crystal was shifted layer by layer along random orientations over 360°. A constant shift magnitude was used.

iii. Structure misorientation. The layers were rotated with rotation axis parallel to the layer stacking direction. The rotation center was placed at the origin of the layer lattice structure. The rotation angle was either defined relative to the nearest neighbor or to the first layer in the stack (i.e., relative to the preceding layer in the stacking sequence or the unperturbed configuration).

iv. Structure shift. The layers were shifted normal to the layer stacking direction (i.e., in-plane with the layer) along random orientations over 360°. A constant shift magnitude was used.

These layer-layer configuration perturbations were either propagated or not in the stacking sequence.

In addition to the unperturbed layer's configuration state, **C**, alternative states were obtained according to the models available from the literature (see **Figure S6A**, **S7A**, **S8A** or **4A**):

Brindley and Robinson (1946).[21] Two additional states were obtained by shift of either $+\mathbf{b}/3$ (state **A**) or $-\mathbf{b}/3$ (state **B**).

Murray (1954).[22] Two additional states were obtained by rotation of the unit structure by ±120°. We slightly adjusted the angles to +120.09° and -119.82° to account for the direction of the mirror plane *n* through the octahedral vacancies in the triclinic cell, which has an angle with the **a**-vector of ~59.91° instead of the ideal 60°.

Newnham and Giese (1961, 1982).[23,24] Although the same configuration states of the Brindley and Robinson model were used, the change of state is limited to $+\mathbf{b}/3$. Therefore, **A→B**, **B→C**, and **C→A** are the only allowed stacking-fault sequences of the states as named for the Brindley and Robinson model.

Plançon and Tchoubar (1977). [25] Vacant and occupied octahedral sites were swapped (i.e., an Al atom was moved to the vacant octahedral site leaving empty (vacant) the previously occupied site). The two Al sites of the kaolinite structure were chosen from the three sites of **Table S2**. The third site left vacant is used to identify the two additional states: **A** and **B**.

Bookin (1989).[26] One additional state was obtained *via* enantiomorphism with the mirror plane *n*.

The configuration states were assumed to change with a constant probability of transition (i.e., stacking-fault probability) from one state to another, and no preferential transition type or long-range correlations were considered.

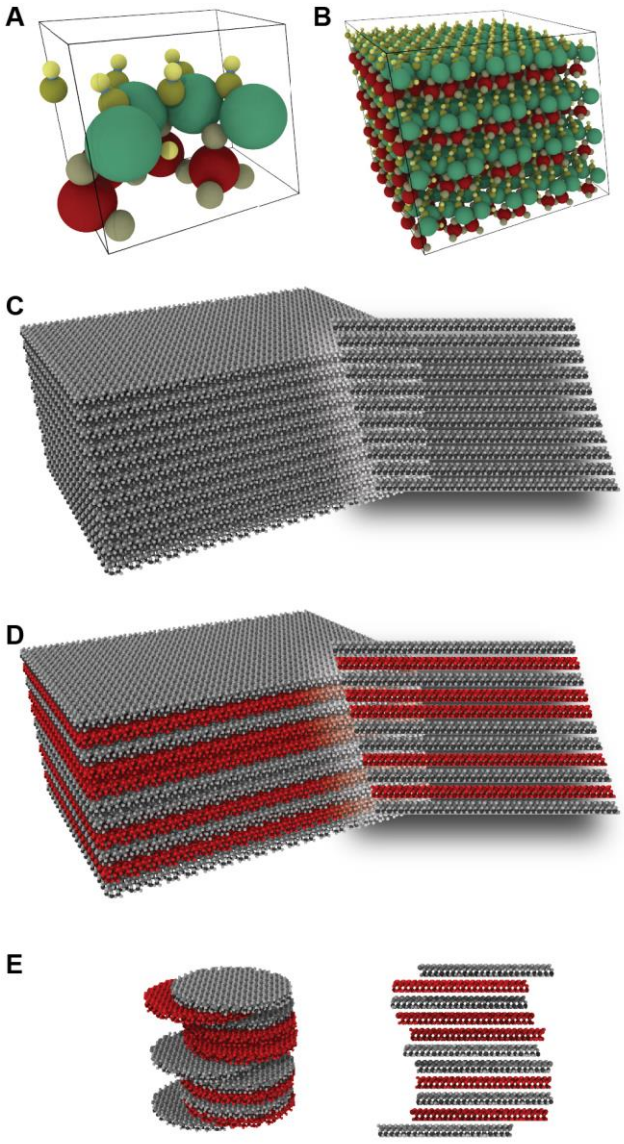

Figure S1. Modelling of kaolinite nanocrystals. From **A** to **B**, the kaolinite unit structure was repeated in space. From **C** to **D**, stacking disorder was incorporated in the infinite perfect crystal. **D**, the red layers highlight a possible set of perturbed layers. From **D** to **E**, finite-size nanocrystals were finally extracted.

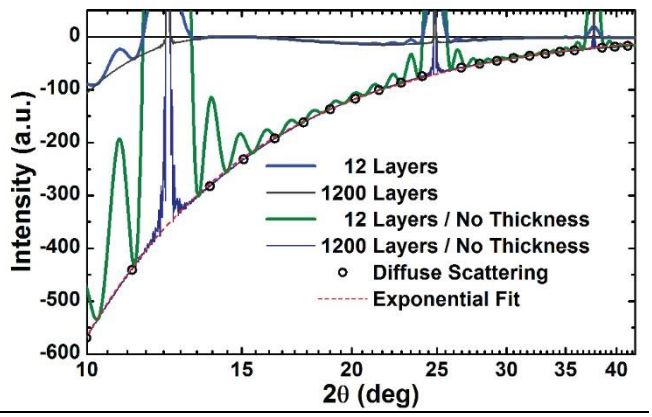

Figure S2. Destructive cross contribution from turbostratic stacking configuration. Although the *ool*-basal peaks becomes sharper with an increasing number of layers, the background destructive contribution remains unchanged. In addition to magnifying both the *ool*-basal reflections and the background profile, neglecting the layer thickness collapses the background to an exponential profile. Profiles from nanocrystals with different layer diameter fully overlap.

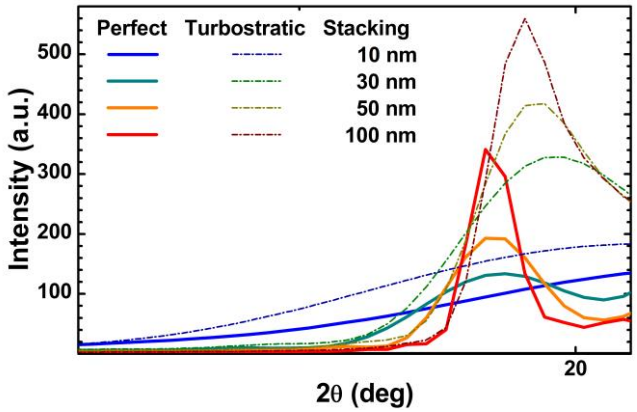

Figure S3. Variation of the *hkl* low-angle tail with layer diameter. The low-angle tails of *hkl* peaks or corresponding reflection bands show an inverse correlation between apparent diffraction angle of the centroid and breadth of the peaks.

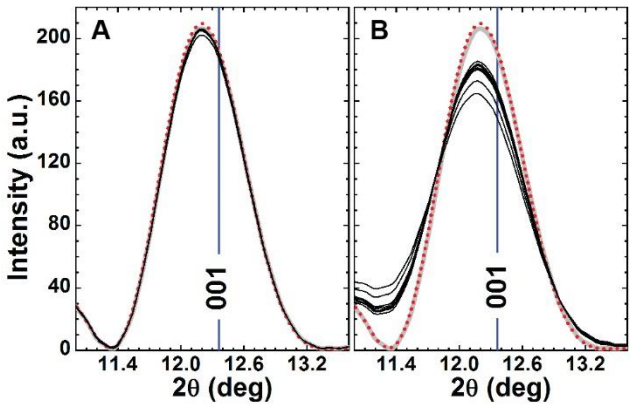

Figure S5. *001* reflection for various dispersions of layer structure misorientation. A, misorientation angle relative to the perfect stacking configuration. **B**, misorientation angle relative to the nearest-neighbor layer. The PXRD profile for the perfect (gray line) and turbostratic (red dot) microstructures are shown as guides for the eye.

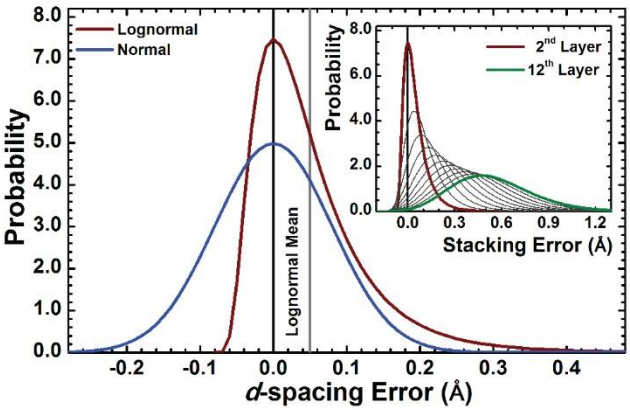

Figure S4. Probability distributions of nearest-neighbor layer *d*-spacing error. The standard deviation of both Gaussian and log-normal (mode equal 0.080 Å) probability distributions was chosen as 0.080 Å. The Lognormal function was shifted to ensure the perfect stacking configuration is the most frequent. As the nearest-neighbor layer *d*-spacing error sums over subsequent interlayers, the stacking error between the bottom and the *n*-th layers is the convolution of the probability function with itself *n* times. Whereas the convolution of two Gaussians is a Gaussian whose variance is the sum of the variances, the inset shows the resulting probability distributions for the Lognormal function.

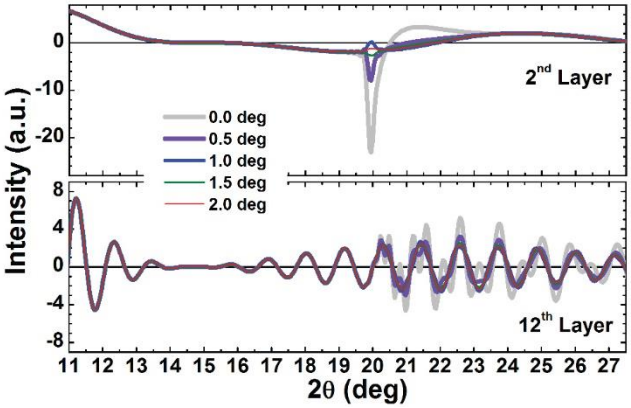

Figure S6. Intensity cross contribution from a pair of misoriented layers. Interference diffraction between the bottom (i.e., 1-st) and the *n*-th layer as a function of the structure misorientation angle.

Figure S7, S8 and S9. A, crystallographic relation between the reference structure (black), the enantiomorphic (red), and the ±120° rotation (green and blue) models. In addition to the unit-cell base (rectangle-like), the **c**-vector (continuous line), and the octahedral sites (circle), the mirror plane *n* (dash-dot line) is also shown. The crystal structure was shifted in the *ab* plane such that the *C* octahedral vacancy is on the c-vector (open circle). Note that the *C* octahedral vacancy is not at the origin of the Cartesian plane because of the inclination of the **c**-vector. **B-F**, Virtual PXRD profiles from defected kaolinite nanocrystals with 12 layers of 50 nm diameter. The PXRD profiles for the perfect (gray line) and turbostratic (red dot) microstructures are shown as guides for the eye. Different stacking-fault models considered were: octahedral sites swap (B), structure shift of $\pm$ **b**/3 or only + **b**/3 (**C** and **D**, respectively), structure rotation of about ±120° (**E**), enantiomorphism (**F**). Note that the rotations of ±120°were adjusted (by less than 0.1°) to consider a triclinic unit cell, which has an angle between the a-vector and the *n* plane slightly out of 60°.

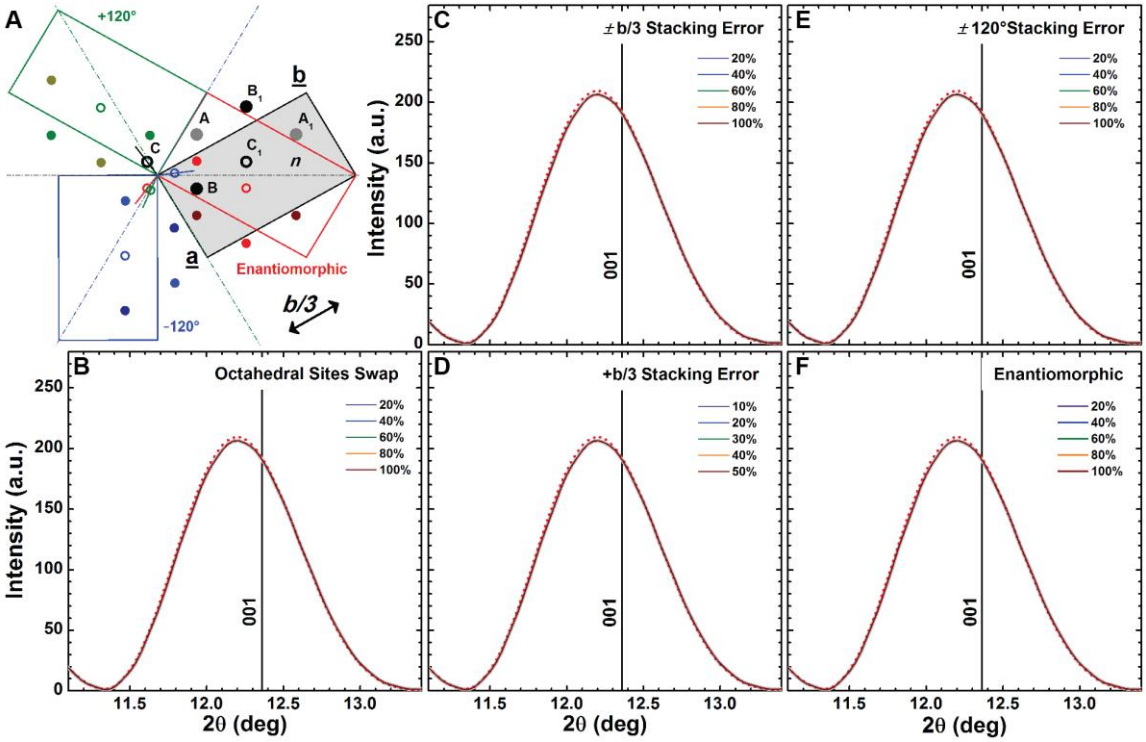

Figure S7. Broadening of the *001* reflection from stacking-fault defects. See above for details.

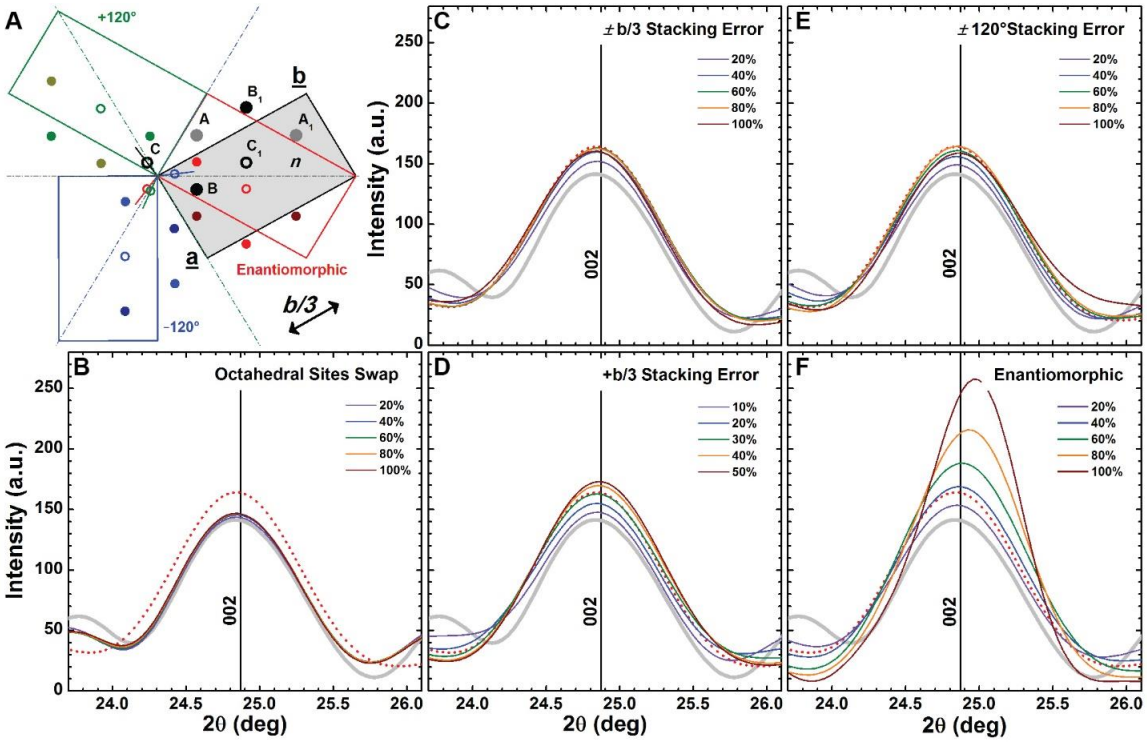

Figure S8. Broadening of the *00ℓ* reflection from stacking-fault defects. See above for details.

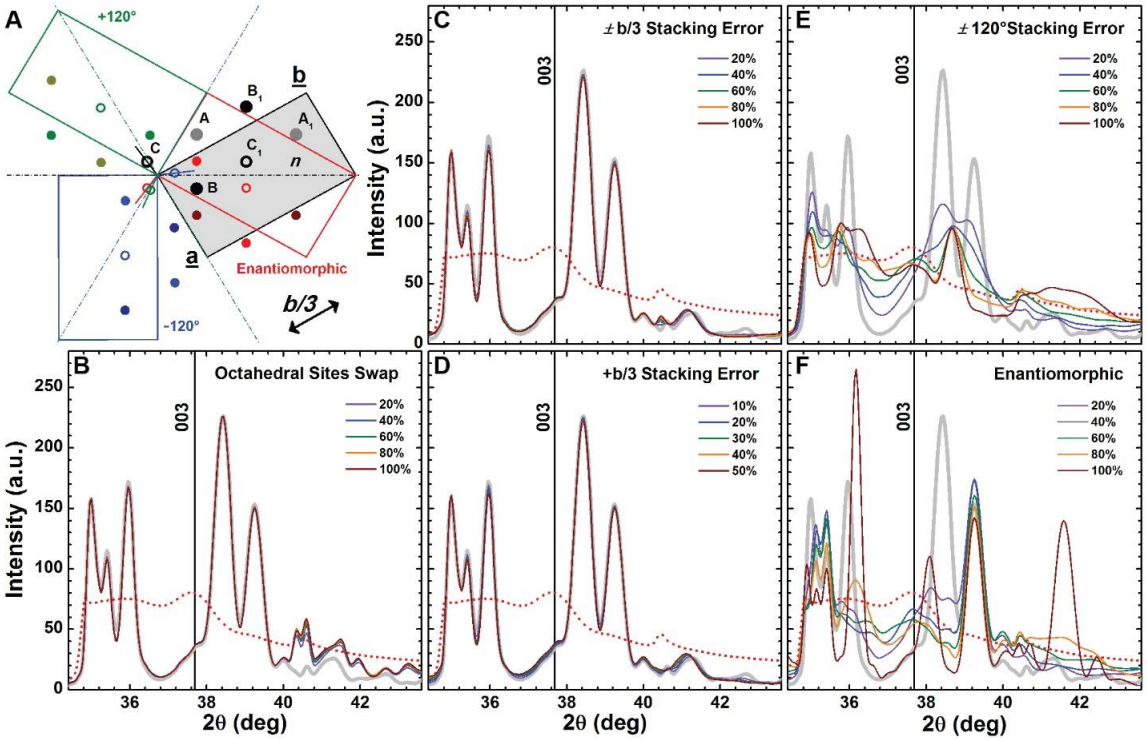

Figure S9. Broadening of the *00ℓ* reflection and nearby *hkl* band from stacking-fault defects. See above for details.

2θ (deg)	API-9 Reference Intensity (a.u.)	Relative Intensity Variation (%)
12.2	10261800000	0
19.8	2285100000	-78
20.1	255225000	-98
20.3	6000960000	-42
20.8	159315000	-98
21.3	5580500000	-46
22.6	51934700	-99
23.1	3760380000	-63
23.7	1655540000	-84
24.8	7573070000	-26
25.8	54434300	-99
26.4	2138310000	-79
27.1	16034300	-100
28.6	558133000	-95
36.0	2165830000	-79
38.4	3281460000	-68
39.3	3593180000	-65
49.5	797096000	-92
50.6	36220600	-100
53.7	518239000	-95
57.9	210614000	-98
63.2	412614000	-96
69.2	261352000	-97
72.2	1245060000	-88
73.2	570192000	-94
76.2	789607000	-92
77.0	905561000	-91
77.5	465563000	-95
78.8	263054000	-97

Table S3. Characteristic diffraction reflections. CuKα 2θ positions of the characteristic diffraction reflections used to estimate the crystallinity index and degree of stacking errors (first column). The intensity from a sample of perfect crystals with size parameters estimated for the API-9 kaolinite standard (second column). The intensity variation from a turbostratic microstructure relative to a perfect microstructure is also provided (third column).

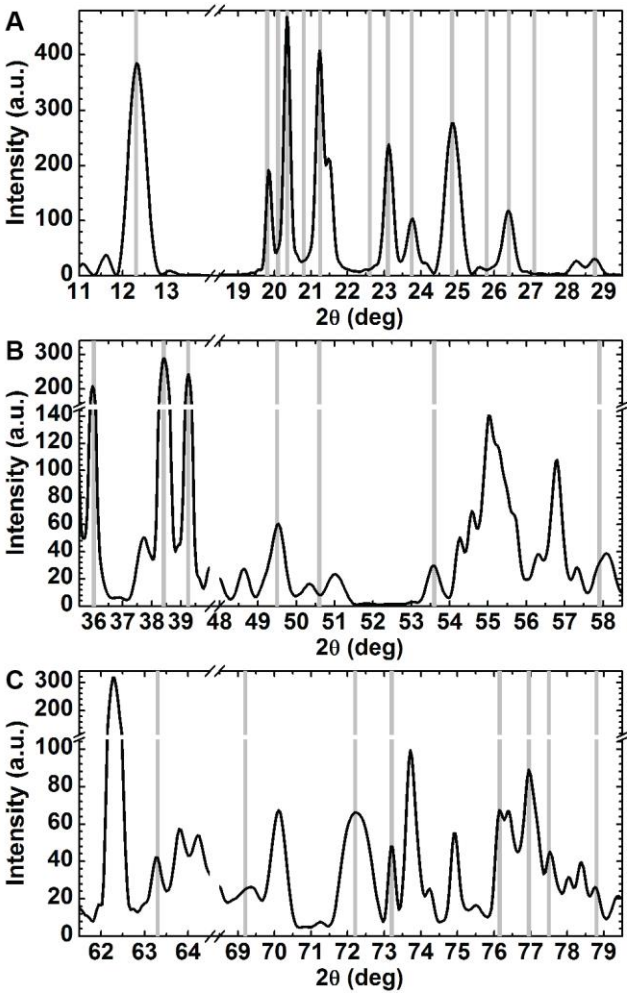

Figure S10. Characteristic diffraction reflections. Positions of the characteristic diffraction reflections used to estimate the crystallinity index and degree of stacking errors (gray lines).

Indentation (%)	Misorientation (deg)	Structure Shift (Å)	Stacking Fault (%)
5.00	0.00	0.00	0.00
10.00	0.05	0.00	0.00
15.00	0.10	0.00	0.00
20.00	0.20	0.00	0.00
25.00	0.30	0.00	1.00
30.00	0.35	0.00	0.00
35.00	0.40	0.05	3.00
40.00	0.55	0.00	0.00
45.00	0.65	0.00	0.00
50.00	0.80	0.00	0.00

Indentation (%)	Misorientation (deg)	Structure Shift (Å)	Stacking Fault (%)
3.00	0.00	0.00	0.00
14.00	0.00	0.00	0.00
25.00	0.00	0.00	0.00
36.00	0.00	0.00	0.00
45.00	0.00	0.00	0.00

Indentation (%)	Misorientation (deg)	Structure Shift (Å)	Stacking Fault (%)
0.00	0.50	0.70	3.00
0.00	1.00	1.10	0.00
0.00	5.00	3.30	13.00
0.00	10.00	3.40	21.00
0.00	15.00	3.45	30.00

Indentation (%)	Misorientation (deg)	Structure Shift (Å)	Stacking Fault (%)
0.00	0.10	0.60	2.00
0.00	8.20	0.30	4.00
0.00	34.00	0.10	0.00

Indentation (%)	Misorientation (deg)	Structure Shift (Å)	Stacking Fault (%)
0.00	0.30	0.50	0.00
0.00	1.00	1.00	0.00
0.50	4.60	1.50	0.00
0.00	8.00	2.00	0.00
0.00	3.40	2.50	0.00
0.00	3.00	3.00	0.00
0.00	8.50	3.50	0.00
0.00	12.00	4.00	0.00
0.00	5.50	4.50	0.00
0.00	4.60	5.0	0.00

Indentation (%)	Misorientation (deg)	Structure Shift (Å)	Stacking Fault (%)
0.00	0.00	0.40	0.00
0.00	0.00	3.70	0.00
0.00	0.30	1.40	0.00
0.00	0.20	4.60	0.00
0.00	0.00	4.60	0.00

Indentation (%)	Misorientation (deg)	Structure Shift (Å)	Stacking Fault (%)
4.00	0.15	0.00	10.0
5.00	0.30	0.00	20.0
25.00	0.20	0.00	30.0
25.00	0.25	0.00	40.0
25.00	0.30	0.00	50.0

Table S4. Correlation between estimated parameters. Disorder parameters estimated neglecting the very type of stacking disorder/error embedded in the kaolinite numerical model. Highlighted in gray are the actual degrees of disorder for the observed models. As expected, almost perfect agreement was found between estimated and actual disorder degree values if the corresponding type was also included in the multivariate analysis.

Indentation (%)	Misorientation (deg)	Structure Shift (Å)	Stacking Fault (%)
0.00	0.00	0.00	12.00
0.00	0.00	0.00	34.00

Table S5. Confidence on estimated parameters. Disorder parameters for a test group of systems. The kaolinite numerical models investigated in this study were separated into a test and a training set. The training set was used for calibration of the multivariate analysis method. Powder X-ray diffraction profiles simulated for the test cases were then analyzed. Raw values are shown in Table S4, mapping the models listed side-by-side.

The estimation of the misorientation degree was affected by the very small (only three) set of training data used. Notably, the degree of indentation was estimated with almost perfect accuracy, and no other disorder/defect type was misinterpreted as this. The estimation of structure-shift was affected by the marked fluctuation of characteristic intensities for small variation of disorder degree compared with the training set intervals.

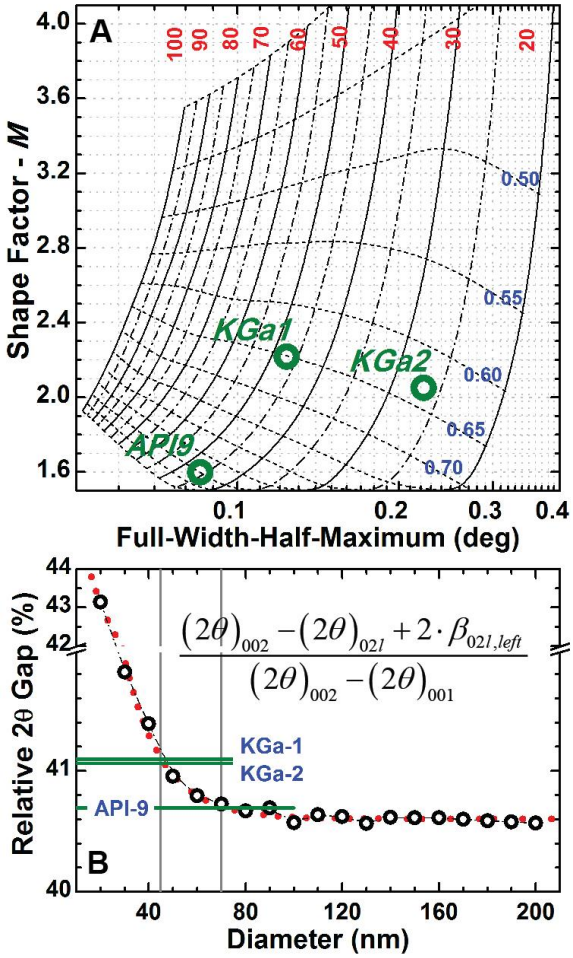

Figure S11. Parametric modification of the PXRD profile as a function of properties for bulk unseparated samples. A, variation of full-width-half-maximum and shape factor (M) of the *002* peak fit with a split Pearson-VII function as a function of the distribution of numbers of layers. **B**, Relative *02l*-*002* 2*θ* gap as a function of the layer diameter. Here *02l* refers to the left tail of the *hkl* band at ~20° CuKα 2*θ*.

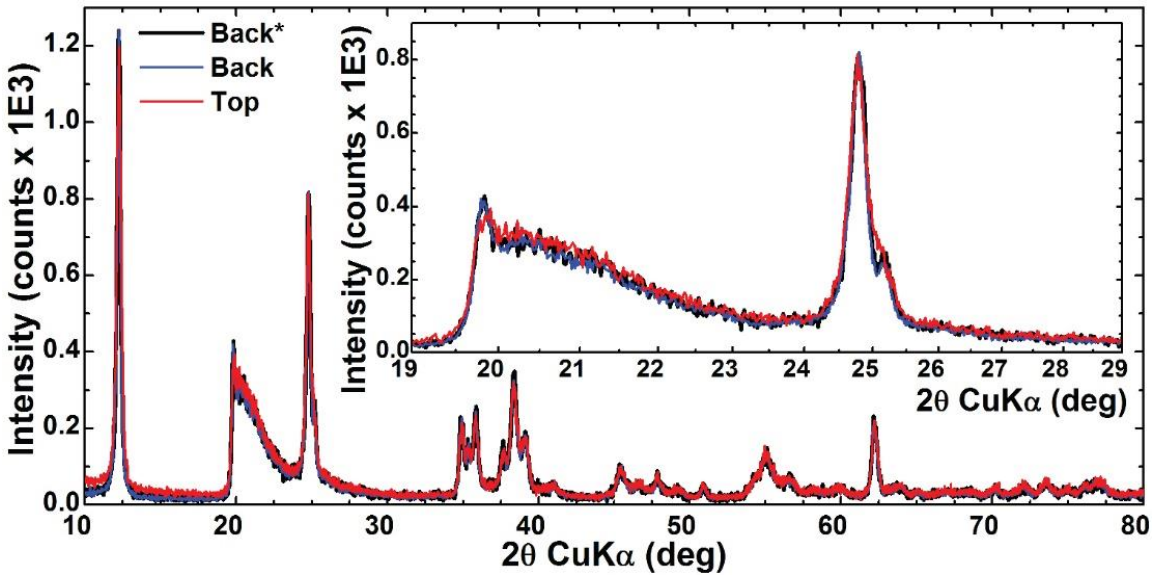

Figure S12. Laboratory powder X-ray diffraction profiles of KGa-2. The profiles were measured adopting different protocols to fill a 1-mm deep cavity flat-plate sample holder. Intensities were rescaled and the diffraction angle shifted (to correct for different specimen displacement) to facilitate comparison of the profiles.

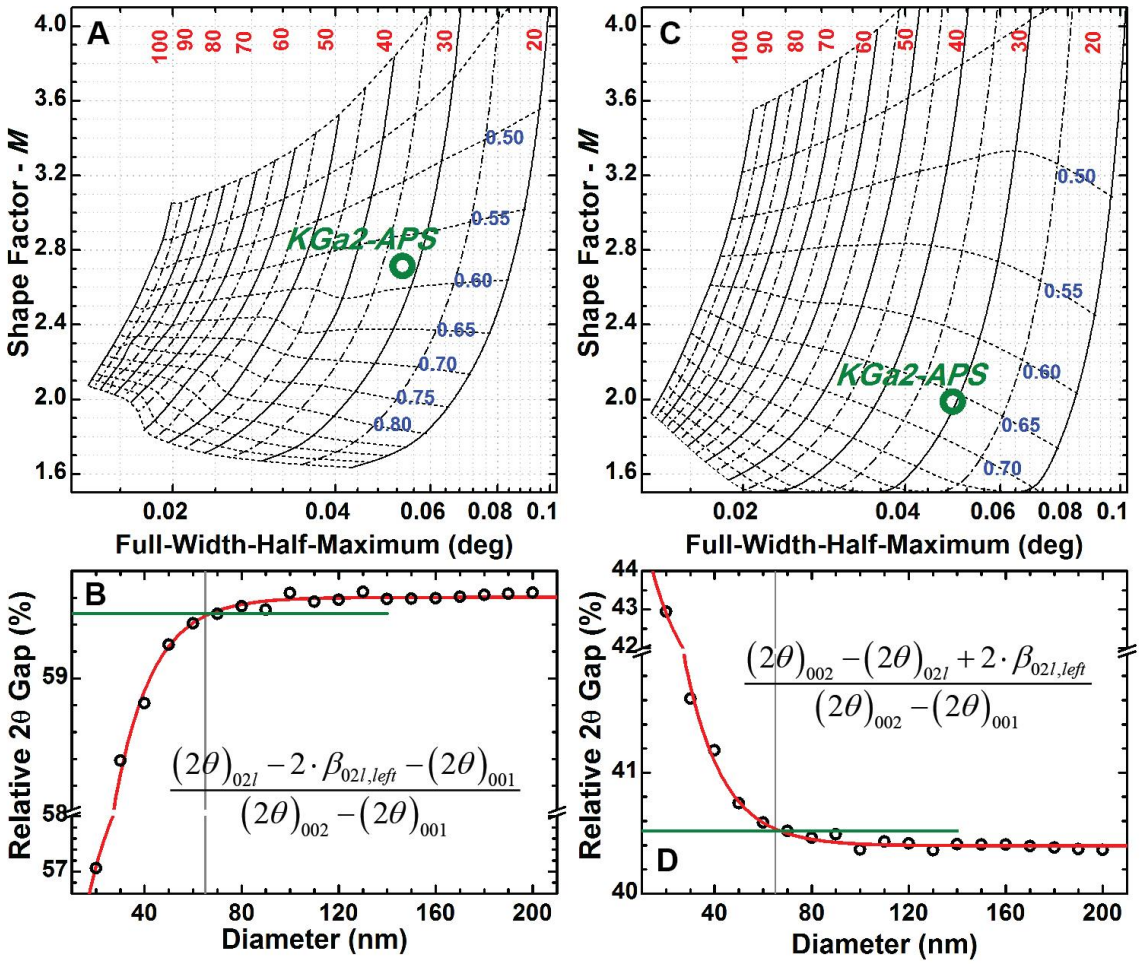

Figure S13. Parametric modification of the PXRD profile as a function of sample properties for data measured with synchrotron radiation. Variation of full-width-half-maximum and shape factor (M) of the 001 (**A**) and 002 (**C**) peaks fit with a split Pearson-VII function as a function of the distribution of number of layers. Relative *02l-001* (**B**) and *002-02l* separation (**D**) 2θ gap as a function of the layer diameter. Here *02l* refers to the left tail of the *hkl* band at ~20° CuKα 2θ.

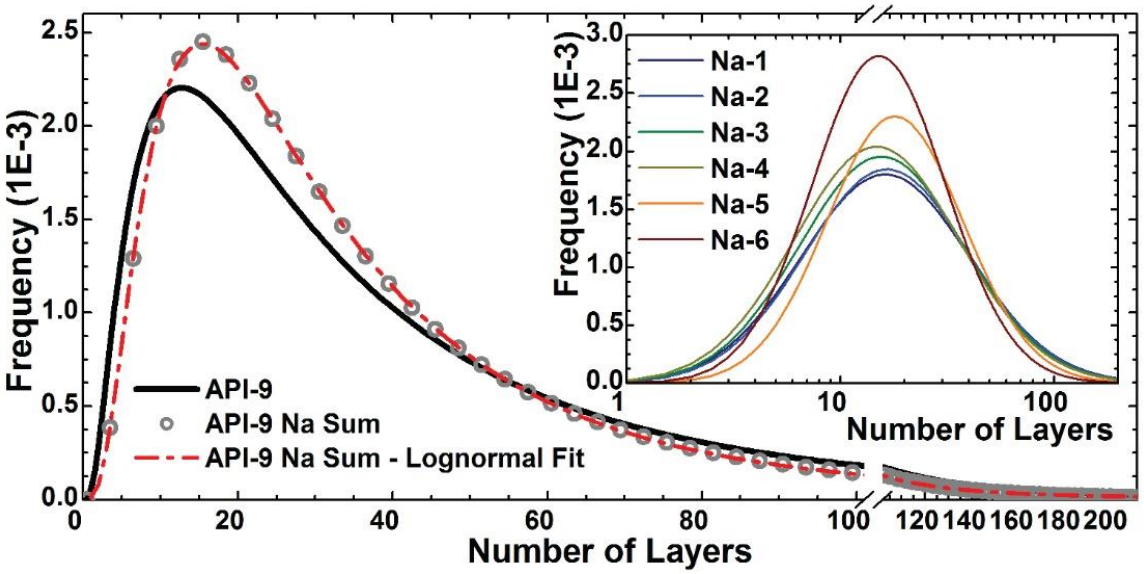

Figure S14. Lognormal distributions of number of layers for the API-9 kaolinite sample. Distribution estimated for the bulk, unseparated sample (black) and as the weighted sum of the distributions from the six particle-size fractions (gray open dots). In the inset are shown the distributions estimated for each of the six particle-size fractions.

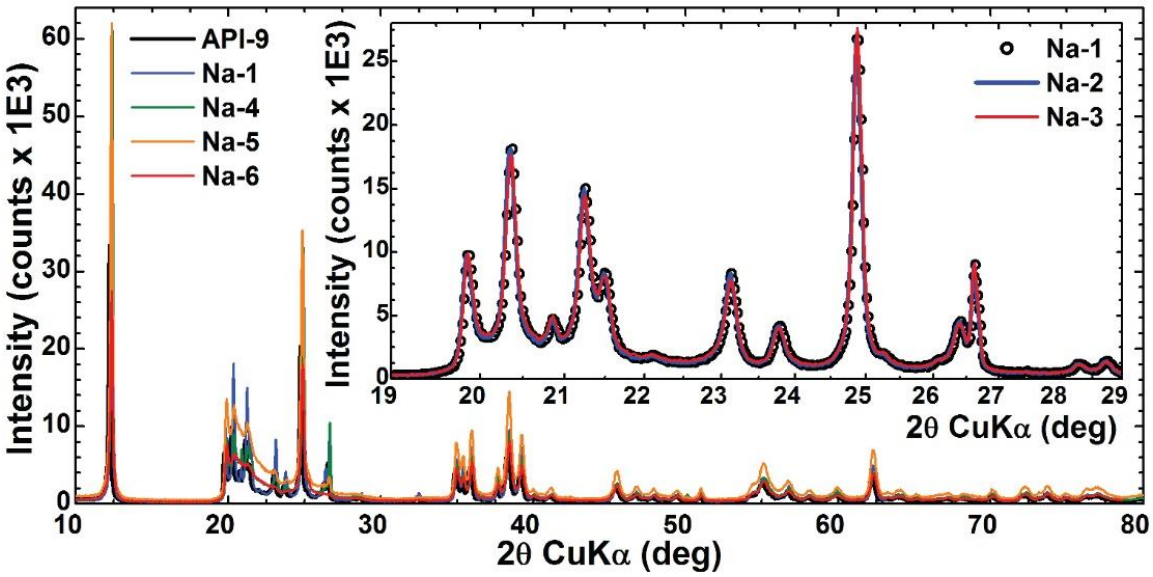

Figure S15. Laboratory powder X-ray diffraction profiles of API-9. The profiles were measured for the standard unseparated sample and for six fractions separated based on particle size. Intensities were rescaled and the diffraction angle shifted (to correct for different specimen displacement) to facilitate comparison of the profiles.

REFERENCES

(1) Rietveld, H. M. Line Profiles of Neutron Powder-Diffraction Peaks for Structure Refinement. *Acta Crystallogr.* **1967**, *22*, 151–152.

(2) Rietveld, H. M. A Profile Refinement Method for Nuclear and Magnetic Structures. *J. Appl. Crystallogr.* **1969**, *2*, 65–71.

(3) Scardi, P.; Leoni, M. Whole Powder Pattern Modelling. *Acta Crystallogr. A* **2002**, *58*, 190–200.

(4) Scardi, P.; Leoni, M.; Dong, Y. H. Whole Diffraction Pattern-Fitting of Polycrystalline Fcc Materials Based on Microstructure. *Eur. Phys. J. B* **2000**, *18*, 23–30.

(5) Warren, B. E.; Averbach, B. L. The Effect of Cold-Work Distortion on X-Ray Patterns. *J. Appl. Phys.* **1950**, *21*, 595–599.

(6) Warren, B. E.; Averbach, B. L. The Separation of Cold-Work Distortion and Particle Size Broadening in X-Ray Patterns. *J. Appl. Phys.* **1952**, *23*, 497–497.

(7) Plançon, A.; Zacharie, C. An Expert System for the Structural Characterization of Kaolinite. *Clay Min.* **1990**, 249–260.

(8) Ufer, K.; Roth, G.; Kleeberg, R.; Stanjek, H.; Dohrmann, R.; Bergmann, J. Description of X-Ray Powder Pattern of Turbostratically Disordered Layer Structures with a Rietveld Compatible Approach. *Zeitschrift fur Krist.* **2004**, *219*, 519–527.

(9) Ufer, K.; Kleeberg, R.; Bergmann, J.; Curtius, H.; Dohrmann, R. Refining Real Structure Parameters of Disordered Layer Structures within the Rietveld Method. *Zeitschrift für Krist. Suppl.* **2008**, *2008*, 151–158.

(10) Ufer, K.; Kleeberg, R.; Bergmann, J.; Dohrmann, R. Rietveld Refinement of Disordered Illite-Smectite Mixed-Layer Structures by a Recursive Algorithm. II: Powder-Pattern Refinement and Quantitative Phase Analysis. *Clays Clay Miner.* **2012**, *60*, 535–552.

(11) Yang, D.; Frindt, R. F. Powder X-Ray Diffraction of Turbostratically Stacked Layer Systems. *Mater. Res.* **1996**, *11*, 1733–1738.

(12) Bergmann, J.; Friedel, P.; Kleeberg, R. BGMN - a New Fundamental Parameters Based Rietveld Program for Laboratory X-Ray Sources, It's Use in Quantitative Analysis and Structure Investigations. *IUCr Comm. Powder Diffr. Newsl.* **1998**, *20*, 5–8.

(13) Ufer, K.; Kleeberg, R.; Monecke, T. Quantification of Stacking Disordered Si–Al Layer Silicates by the Rietveld Method: Application to Exploration for High-Sulphidation Epithermal Gold Deposits. *Powder Diffr.* **2015**, *30*, S111–S118.

(14) Treacy, M. M. J.; Newsam, J. M.; Deem, M. W. A General Recursion Method for Calculating Diffracted Intensities from Crystals Containing Planar Faults. *Proc. R. Soc. A Math. Phys. Eng. Sci.* **1991**, *433*, 499–520.

(15) Leoni, M.; Gualtieri, A. F.; Roveri, N. Simultaneous Refinement of Structure and Microstructure of Layered Materials. *J. Appl. Crystallogr.* **2004**, *37*, 166–173.

(16) Jiang, Y.; Cao, L.; Hu, X.; Ren, Z.; Zhang, C.; Wang, C. Simulating Powder X-Ray Diffraction Patterns of Two-Dimensional Materials. *Inorg. Chem.* **2018**, *57*, 15123–15132.

(17) Drits, V. A.; Tchoubar, C. *X-Ray Diffraction by Disordered Lamellar Structures*; Springer: Berlin, 1990.

(18) Sakharov, B. A.; Drits, V. A.; McCarty, D. K.; Walker, G. M. Modeling Powder X-Ray Diffraction Patterns of the Clay Minerals Society Kaolinite Standards: Kga-1, Kga-1b, and Kga-2. *Clays Clay Miner.* **2016**, *64*, 314–333.

(19) Drits, V.; Środoń, J.; Eberl, D. D. XRD Measurement of Mean Crystallite Thickness of Illite and Illite/Smectite: Reappraisal of the Kubler Index and the Scherrer Equation. *Clays and Clay Minerals*. 1997, pp 461–475.

(20) Bish, D. L.; Dreele, R. B. Von. Rietveld Refinement of Non-Hydrogen Atomic Positions in Kaolinite. *Clays Clay Miner.* **1989**, *374*, 289–296.

(21) Brindley, G. W.; Robinson, K. Randomness in the Structures of Kaolinitic Clay Minerals. *Trans. Faraday Soc.* **1946**, *42*, B198.

(22) Murray, H. Structural Variations of Some Kaolinites in Relation to Dehydrated Halloysite. *Am. Mineral.* **1954**, *39*, 97–108.

(23) Newnham, R. E. A Refinement of the Dickite Structure and Some Remarks on Polymorphism in Kaolin Minerals. *Mineral. Mag. J. Mineral. Soc.* **1961**, *32*, 683–704.

(24) Giese, R. F. Theoretical Studies of the Kaolin Minerals: Electrostatic Calculations. *Bull. Mineral.* **1982**, *105*, 417–424.

(25) Plançon, A.; Tchoubar, C. Determination of Structural Defects in Phyllosilicates by X-Ray Powder Diffraction—II. Nature and Proportion of Defects in Natural Kaolinites. *Clays Clay Miner.* **1977**, *25*, 436–450.

(26) Bookin, A. S.; Drits, V. A.; Plançon, A.; Tchoubar, C. Stacking Faults in Kaolin-Group Minerals in the Light of Real Structural Features. *Clays Clay Miner.* **1989**, *37*, 297–307.